

Multiple-scattering lidar from both sides of the clouds: Addressing internal structure

A. B. Davis¹

Received 1 December 2007; revised 17 March 2008; accepted 19 May 2008; published 31 July 2008.

[1] Multiple-scattering (a.k.a. “off-beam”) lidar is an emerging technology in cloud remote sensing. It delivers, as in classic lidar ceilometry, cloud base altitude but also the cloud’s physical thickness H as well as its optical depth τ (averaged over horizontal scales on the order of H). The value of τ in fact must lie beyond the range accessible by standard (i.e., single-scattering/on-beam) lidar profiling, namely, up to 3–4. A refined diffusion-theoretical model is presented here for signals from multiple-scattering lidar and applied, on the one hand, to retrieval algorithm development and, on the other hand, signal-to-noise ratio (SNR) estimation. SNRs are computed for LANL’s ground-based Wide-Angle Imaging Lidar (WAIL) system and NASA’s space-based Lidar-In-space Technology Experiment (LITE). The refinements are threefold and all about internal structure. First, the laser source is modeled as a collimated anisotropic exponentially distributed internal source rather than an isotropic point source at the cloud boundary; this opens the possibility of using δ -Eddington rescaling to capture the forward peaked phase function more effectively within the diffusion framework. Second, stratification of the scattering coefficient is modeled as an increasing function of distance to cloud base; this strongly differentiates the signals when observed from above or from below. Finally, Cairns’ rescaling is applied to this conservative scattering problem to account for the systematic effects of random (turbulence-driven) internal variability at scales up to a few mean free paths.

Citation: Davis, A. B. (2008), Multiple-scattering lidar from both sides of the clouds: Addressing internal structure, *J. Geophys. Res.*, 113, D14S10, doi:10.1029/2007JD009666.

1. Motivation, Context, and Outline

[2] It is commonplace to say that getting clouds right is an essential step in predictive climate science at both regional and global scales, for both near- and long-term forecasts. They are obvious elements in the radiation budget and hydrological cycle. They also participate actively in atmospheric aerosol processes, including their intricate chemistry in the aqueous phase as well as reactions on the surfaces offered by cloud particles [Ghan and Schwartz, 2007]. It is not as frequently voiced that clouds remain a significant challenge in remote sensing, and remote sensing is the only way we can assess them statistically with reasonable space-time sampling. As much as one would like to view clouds as known (or at least readily knowable) quantities, efforts with national and international reach such as DOE’s Atmospheric Radiation Measurement (ARM) program are predicated on the fact that we need to improve our knowledge and understanding of clouds. In recent years, it has become clear that possibly the strongest, and certainly the most uncertain, impacts of anthropogenic aerosol on the climate are mediated one way or another by clouds

[Solomon *et al.*, 2007]. The aerosol-cloud-radiation-climate problem indeed motivated much of Yoram Kaufman’s scientific work and dominates this special section of *Journal of Geophysical Research—Atmospheres*.

[3] Even though they are zeroth-order, questions about where we locate cloud boundaries, and the associated issue of cloud fraction, are already difficult. Part of this difficulty is that the answer depends inherently on the observational approach. And it should! Indeed, the spatial transition from clear to cloudy air is made fuzzy by nature herself through the complex interplay between advective and convective dynamics, thermodynamics, nucleation, turbulence, radiation, and so on, as any cloud modeler is well aware. It is therefore important to decide what instrumentation is best adapted to a given application that requires knowledge of cloud boundaries. This recommendation still stands when one asks the first-order question about what is going on inside the cloud boundaries in terms of instantaneous distributions of liquid and ice water content.

[4] Only after a cloud probing technique is selected, can one start meaningful discussions about precision, accuracy, robustness, reliability, sampling, etc. For instance, if climate modeling is the primary goal, then it is probably best to use remote sensing instrumentation that operates at wavelengths that matter most for the radiation budget; otherwise, a theory-based extrapolation across the EM spectrum is in order and this adds a vulnerability to the climate model.

¹Space and Remote Sensing Group, Los Alamos National Laboratory, Los Alamos, New Mexico, USA.

Although there are many good reasons to invest large resources into radar and microwave technologies [e.g., Stephens, 1994], it is also important to keep working on passive and active techniques in the VIS through thermal IR region of the spectrum. Ultimately, we must recognize that, since different instruments “see” clouds differently, comprehensive observation of clouds for multiple purposes mandates multi-instrumental synergy and, if necessary, cloud data fusion.

[5] In this paper and its companion (A. B. Davis et al., Multiple-scattering lidar from both sides of the clouds: LITE from above, WAIL from below, manuscript in preparation, 2008, hereinafter referred to as Part 2), we revisit active remote sensing in the optical (VIS and Near-IR) spectrum, i.e., lidar, from a cloud perspective. The attending radiative transfer (RT) is dominated by scattering and the fundamental radiation transport physics will range from a ballistic/single-scattering regime to slow diffusion through extended regions where opacity is high, hence mean free paths (MFPs) are small. So far, atmospheric lidar has assumed the former situation. So much so that the famous “lidar equation” which predicts the lidar signal for a given atmospheric profile is an expression of two-way direct transmission and a single scattering through 180° (we assume here a so-called monostatic configuration where the transmitter and receiver are side by side, or even integrated as in micropulse lidars [Spinhirne, 1993]). In this case, the main constraint on the optical design is that the detector field of view (FOV) should contain all of the laser beam at all the ranges of interest; otherwise an “overlap function” must be determined and applied (at the cost of lost signal). Consequently, standard lidar FOVs are quite small, commensurate with the (typically diffraction-limited) divergence of the laser beam, on the order of a few mrad. For obvious reasons, this type of propagation will only cross the most tenuous clouds and penetrate only the first layers of their dense counterparts.

[6] We explore here the opposite asymptotic limit of RT where the lidar signal is dominated by beams energized by the multiple scattering source function. Once the cloud boundary nearest to the pulsed laser source is detected and ranged, this new signal modeling framework has no place for the ranging part of LIDAR (Light Detection and Ranging). However, it opens up new opportunities for cloud probing all the way to the nonilluminated boundary which may be very many MFPs away from the laser source. See schematic in Figure 1. In this scenario, the main constraint on the optical design is that the receiver FOV should contain as much as possible of the spatial pattern of reflected light excited by the laser beam. It has been shown theoretically [Marshak et al., 1995] and observationally [Davis et al., 1997] that, in reflection, the root-mean-square (RMS) radius of this radiative Green function is commensurate with the harmonic mean of the cloud thickness H , \sim km, and the “transport” MFP ℓ_t , \sim 100 m. (ℓ_t and H are the natural inner and outer scales of diffusion theory. Letting g be the asymmetry factor and τ the cloud optical depth, their ratio is $(1 - g)\tau$ and we can moreover take $g \approx 0.85$ for all clouds of interest here.) We are thus contemplating an RMS radius of \sim 0.3 km and a FOV that captures at least one full kilometer at cloud level; at typical ranges from ground, \sim 1 km, this can translate to \sim 1 radian, preferably even more.

[7] Curiously, multiple scattering in space-based lidar observations of clouds elicited strong interest [Flesia and Schwendemann, 1995; Miller and Stephens, 1999] before the same signal physics was investigated systematically for systems at much closer range to the cloud, either ground-based [Davis et al., 1999; Love et al., 2001a; Polonsky et al., 2005] or airborne [Cahalan et al., 2005]. A novel and interesting development is the idea that the multiple-scattering lidar system can be embedded in the cloud [Evans et al., 2003, 2006]. Originally, multiple scattering in lidar was generally viewed as a nuisance, and compensation methodology was developed to restore the utility of the single-scattering lidar equation. As far as we know, the first thrust in signal modeling and instrument development based on the notion that the multiple scattering component of the lidar signal can be useful was advanced by Bissonnette et al. [2002, and references therein] and described as “Multiple Field-Of-View” (MFOV) lidar; apart from standard ranging and quantifying aerosol density fluctuations, MFOV gives access to information on particle size distributions.

[8] To summarize, lidar is generally viewed as a mature technology addressing the atmospheric aerosol with unprecedented spatial and temporal detail, and now organized into growing networks in Europe, North and South America, and Asia that will in time be federated into a global network of networks. This growth and effort in standardization will lead to lidar data assimilation into NWP, regional and global transport studies, improved air quality forecasts, and so on. The new class of cloud-probing instruments supported by the present modeling study are bridging the gap between aerosol and clouds using the very same wavelengths and closely related detector physics. Conceivably, lidars with dense cloud capability will populate the same networks worldwide, capitalizing on the same investment in infrastructure; in some cases, the same transmitter may be used and only an extra detector will be added at a relatively low cost. In time, this kind of sensor development will help to bring on the scientific breakthrough we need to fully understand cloud-aerosol interaction. Active probing of both atmospheric components of the climate system with essentially the same instrumentation, the only difference being in the data collection and analysis, is a step in the right direction.

[9] The paper is dedicated to the forward modeling of the multiple-scattering lidar (MSL) signal using every resource radiative diffusion theory can bring to bear. In the following section, we review the rigorous time-dependent 3-D RT theory that supports MSL concepts in dense cloud remote sensing, up to the definition of space-time moments that play a key role in MSL signal phenomenology. In section 3, we establish a general diffusion-theoretical framework for multiple-scattering cloud lidar signal prediction. In section 4, we present diffusion results using a new and improved representation of the pulsed laser source, now as an internal distribution with the full degree of anisotropy allowed in diffusion theory; for illustration, we apply it to a moment-based retrieval scheme. In section 5, we introduce two new cloud parameters (beyond H and τ) that describe internal cloud structure: one describes a macroscale gradient in opacity from bottom to top, and the other [adapted from Cairns et al., 2000] describes microscale random variability. In section 6, we apply this body of theory to the estimation of

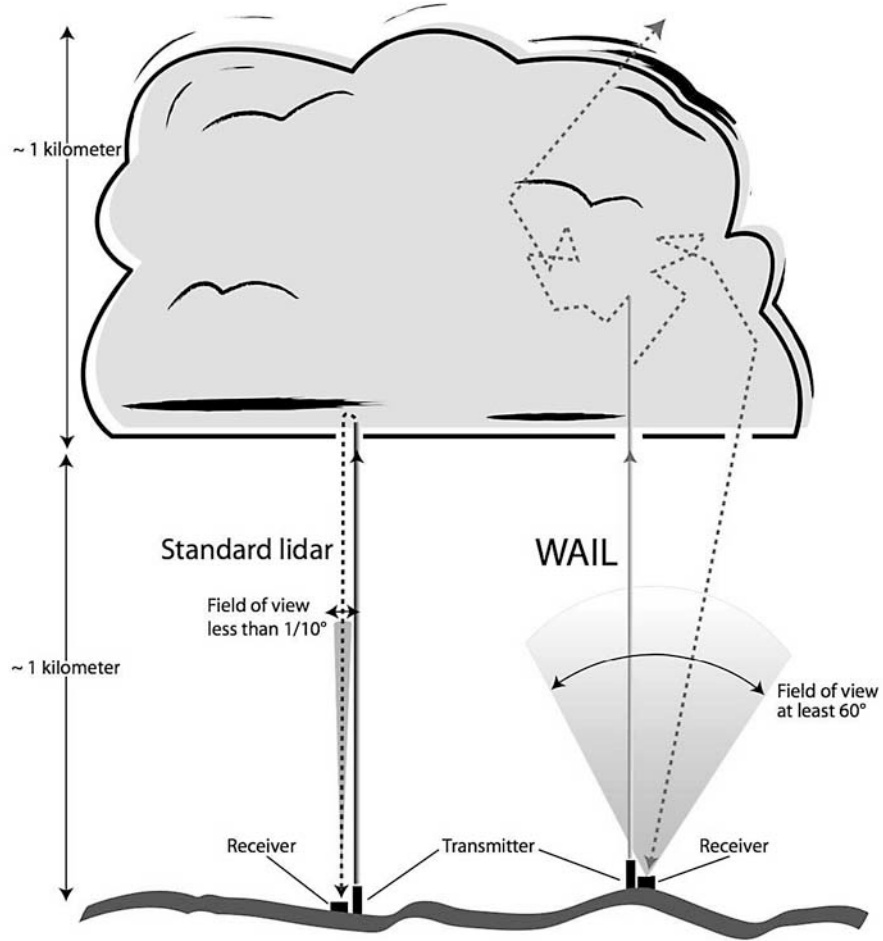


Figure 1. Lidar observation of a dense cloud. Standard (single-scattering/on-beam) lidar is illustrated on the left, and multiple-scattering/off-beam lidar is illustrated on the right. We note the narrowness of the FOV in the standard case, as is required to restrict as much as possible the signal to a single backscatter, and the very wide FOV in the case of off-beam lidar, designed to capture all orders of scattering in the reflected laser light.

the raw MSL signal magnitude, and associated noises, for two radically different multiple-scattering cloud lidar systems. We summarize our results in section 7.

2. Preliminary Radiative Transfer and Probability Theory

2.1. A New Lidar Equation

[10] A pulsed laser is for all practical purposes a physical instantiation of a Dirac δ source of illumination in time t , 3-D space \mathbf{r} , propagation direction $\mathbf{\Omega}$, as well as wavelength and possibly even polarization. By definition, the radiation field it excites is therefore a Green function $G(t, \mathbf{r}, \mathbf{\Omega})$, the governing time-dependent 3-D RT equation being

$$\left[c^{-1} \frac{\partial}{\partial t} + \mathbf{\Omega} \cdot \nabla + \sigma(z) \right] G = \sigma_s(z) \int_{4\pi} p(\mathbf{\Omega}' \cdot \mathbf{\Omega}) \cdot G(t, \mathbf{r}, \mathbf{\Omega}') d\mathbf{\Omega}' + Q(t, \mathbf{r}, \mathbf{\Omega}), \quad (1)$$

where we balance sinks on the left-hand side (LHS) and sources on the right-hand side (RHS) for the time-dependent

radiance field in a small volume along beam direction $\mathbf{\Omega}$. From left to right, we recognize the negative imprints of advection (total derivative $c^{-1} \partial_t + \mathbf{\Omega} \cdot \nabla$) and extinction, and positive counterparts for in-scattering and volume emission. Scattering and extinction coefficients are denoted $\sigma_s(z)$ and $\sigma(z)$ respectively and assumed to vary only in the vertical, but maintaining a constant ratio ϖ_0 . The scattering phase function $p(\mathbf{\Omega}' \cdot \mathbf{\Omega})$ is assumed axisymmetric (we will not concern ourselves here with cirrus) and spatially uniform. The complementary coefficient, $\sigma_a(z) = \sigma(z) - \sigma_s(z) = (1 - \varpi_0)\sigma(z)$, captures absorption processes as needed. As in most atmospheric RT texts, we denote $\mathbf{\Omega}(\theta, \phi) = (\eta \cos \phi, \eta \sin \phi, \mu)^T$ in Cartesian coordinates using polar angles, where $\mu = \cos \theta$ and $\eta = \sqrt{1 - \mu^2}$.

[11] We can assume no incoming radiance at the cloud boundaries and model the laser source internally as

$$Q(t, \mathbf{r}, \mathbf{\Omega}) = E_p \delta(x) \delta(y) \delta(t - z/c) \sigma_s(z) p(\mu) \cdot \exp \left(- \int_0^z \sigma(z') dz' \right), \quad 0 < z < H, \quad (2)$$

assuming vertical (z axis) beam alignment, a plane-parallel cloud of thickness H at right angles, and total pulse energy E_p . Note from the writing of the third δ function that the instant $t = 0$ is when the laser pulse hits the cloud boundary at $z = 0$, precisely at $x = y = 0$. In this case, the direct beam is treated separately from the diffuse radiance field. Only the later is of interest in lidar on the detection side.

[12] Alternatively, we can set $Q(t, \mathbf{r}, \mathbf{\Omega}) \equiv 0$ and model the highly directional laser source in the explicit statement of boundary conditions (BCs):

$$\begin{aligned} G(t, x, y, 0, \mathbf{\Omega}) &= E_p \delta(t) \delta(x) \delta(y) \delta(\mathbf{\Omega} - \hat{\mathbf{z}}), \quad \mu > 0, \\ G(t, x, y, H, \mathbf{\Omega}) &= 0, \quad \mu < 0. \end{aligned} \quad (3)$$

where $\hat{\mathbf{z}}$ orients the positive z axis. In this case, the resulting radiance field contains both direct and diffuse components. Apart from this interpretation of what is contained in $G(t, \mathbf{r}, \mathbf{\Omega})$ or not, the two ways of modeling the pulsed laser source are equivalent. Either way, we have now entirely determined the radiation transport in MSL.

[13] However, in this particular application, we are only interested in the reflected diffuse field at the illuminated boundary: $G(t, x, y, 0, \mathbf{\Omega})$, when $\Omega_z = \mu < 0$. More precisely, we assume an imaging detector is measuring this radiance at some finite standoff distance $d_{\text{obs}} > 0$ from the illuminated cloud boundary; that is, the MSL sensor is positioned at $\mathbf{r}_{\text{obs}} = (0, 0, -d_{\text{obs}})^T$. We denote the time-dependent cloud response at the detector $I(t_{\text{round-trip}}, \theta_{\text{obs}})$ where, by axial symmetry around the laser beam, we have no dependence on the azimuthal angle. From this vantage point, we subsample the axisymmetric boundary Green function for boundary illumination, $G(t, x, y, 0, \mathbf{\Omega}) \equiv G(t, \rho, 0, \mathbf{\Omega}_{\text{obs}}(\rho))$ where

$$\begin{aligned} t &= t_{\text{round-trip}} - (1 + 1/\cos \theta_{\text{obs}})d_{\text{obs}}/c, \\ \rho(\theta_{\text{obs}}) &= \sqrt{x^2 + y^2} = d_{\text{obs}} \tan \theta_{\text{obs}}, \\ \text{hence, } \theta_{\text{obs}}(\rho) &= \tan^{-1}(\rho/d_{\text{obs}}), \\ \text{and } \mathbf{\Omega}_{\text{obs}}(\rho) &= (-\sin \theta_{\text{obs}}(\rho), 0, -\cos \theta_{\text{obs}}(\rho))^T. \end{aligned} \quad (4)$$

We assume here, for simplicity, that radiance is sampled in the $y = 0$ half-plane with $\rho = x \geq 0$ ($\phi = 0$). By deriving $I(t_{\text{round-trip}}, \theta_{\text{obs}}(\rho))$ from $G(t, \rho, 0, \mathbf{\Omega}_{\text{obs}}(\rho))$ and $d_{\text{obs}} < \infty$ using (1) and (4), with either (2) or (3) to describe the source, we have completely specified the new lidar equation for multiple-scattering systems in the framework of RT theory.

[14] To illustrate this point with standard/on-beam lidar, we compute only the single-scattering term; using (2) and the well-known propagation kernel for (1), we have

$$\begin{aligned} I_1(t + 2d_{\text{obs}}/c) &= \int_{-\infty}^{+\infty} \int_{-\infty}^{+\infty} \int_0^H Q(t, x, y, z, -\hat{\mathbf{z}}) \\ &\quad \exp\left(-\int_0^z \sigma(z') dz'\right) \\ &\quad \cdot \frac{1}{(z + d_{\text{obs}})^2} dx dy dz, \\ &= E_p c \sigma_s(z) p(-1) \frac{\exp\left(-2 \int_0^z \sigma(z') dz'\right)}{(z + d_{\text{obs}})^2} \Bigg|_{z=ct}, \end{aligned} \quad (5)$$

for a uniform medium. The exponential term decays very rapidly over a few MFPs (recalling that $1 \text{ MFP} = 1/\sigma$), and therein is the limitation of penetration by standard lidar into dense clouds. In MSL, by contrast, we are interested in the full solution of the 3-D RT equation.

[15] In the limit $d_{\text{obs}} \rightarrow \infty$, a reasonable approximation for an orbital detector, the connections in (4) still make sense by taking the simultaneous limit $\theta_{\text{obs}} \rightarrow 0$, keeping ρ constant. We thus denote the detector response as $I(t, \rho)$, after accounting for the large but finite time delay, and the last connection simplifies to $\mathbf{\Omega}_{\text{obs}}(\rho) \equiv -\hat{\mathbf{z}}$.

2.2. Spatial and Temporal Moments

[16] To summarize the above, we need to obtain from theory, computation, remote lidar measurements, or some combination of the above, the time-dependent axisymmetric (equivalent) reflectance field $R_{\text{obs}}(t, \rho) = \pi G(t, \rho, 0, \mathbf{\Omega}_{\text{obs}}(\rho))/E_p$, which is normalized by the pulse energy. Temporarily ignoring angular sampling and truncation issues in real measurements, we define

$$R(t, \rho) = \frac{2\pi}{E_p} \int_{\pi/2}^{\pi} |\cos \theta| G(t, \rho, 0, \mathbf{\Omega}(\theta, 0)) \sin \theta d\theta, \quad (6)$$

as the local time-dependent reflected flux field.

[17] Largely to improve the signal-to-noise ratio (see section 6), it is of interest to use spatial and/or temporal integrals of the observed $R(t, \rho)$. We are particularly interested in its statistical moments when it is viewed as a probability density function (PDF) for escape in reflection. We will therefore estimate:

$$R = 2\pi \int_0^{\infty} dt \int_0^{\infty} R(t, \rho) \rho d\rho, \quad (7)$$

the cloud's albedo (for steady, uniform and normal illumination), and moments

$$\langle t^q \rangle = \frac{2\pi}{R} \int_0^{\infty} t^q dt \int_0^{\infty} R(t, \rho) \rho d\rho \quad (q = 1, 2, \dots), \quad (8)$$

$$\langle \rho^2 \rangle = \frac{2\pi}{R} \int_0^{\infty} dt \int_0^{\infty} \rho^2 R(t, \rho) \rho d\rho. \quad (9)$$

Angular brackets will always denote an average over space and/or time.

[18] Note that the moment estimations in (9)–(8) are immune to uncertainties in a multiplicative constant for $R(t, \rho)$. From an observational standpoint, and in sharp contrast with the estimation of cloud albedo in (7), absolute calibration is not required. But the easier task of flat-fielding of the imager's focal plane array is necessary.

[19] Of course, real-world MSL observations give us no information on $G(t, \rho, 0, \mathbf{\Omega}_{\text{obs}}(\rho))$, hence on $R(t, \rho)$, outside of the receiver's FOV (i.e., the actual upper limit of all the

above integrals over ρ is finite). Moreover, for each value of ρ we only get one value of θ in (4). The latter problem is resolved by using an angular model to convert an observed radiance into a boundary flux. The former problem is best addressed by designing MSL instruments with the widest possible FOV, such that it contains at least a couple of the Green function's e-folding distances away from the axis; we can then assume that the residual truncation in both numerators and denominators in (9)–(8) does not bias the estimates. We return to these two observational issues respectively in sections 3.3 and 6.1.

2.3. Moment Estimation in Fourier-Laplace Space

[20] Moment integrals in (8)–(9) are easy to compute by manipulation of transforms in Fourier-Laplace space. In probability theory, the Fourier or Laplace transforms of a PDF is called its “characteristic” or “moment-generating” function. Which transform is used depends on the support of the PDF. In our application, we need both Laplace for time $t \in [0, \infty)$ and 2-D Fourier for position $\vec{\rho} = (x, y)^T \in \mathbb{R}^2$ in the $z = 0$ plane.

[21] We are thus interested in

$$\begin{aligned} \tilde{R}(s, \vec{k}) &= \int_0^\infty dt \int_{-\infty}^{+\infty} \int_{-\infty}^{+\infty} \exp(-st + i\vec{k} \cdot \vec{\rho}) G(t, \vec{\rho}, z) dx dy \\ &= R \times \langle \exp(-st + i\vec{k} \cdot \vec{\rho}) \rangle \end{aligned} \quad (10)$$

for the time-dependent 2-D reflectance field. It is not hard to see that coefficients of Taylor expansions of $\tilde{R}(s, \vec{k})$ at $s = 0$ and $\vec{k} = \vec{0}$ can be used to compute spatial and temporal moments. By translational and rotational symmetries that carry over from physical to Fourier space, we have $\tilde{R}(s, \vec{k}) \equiv \tilde{R}(s, k)$ and, specifically, we need to compute albedo $R = \tilde{R}(0, 0)$, as well as moments

$$\langle t^q \rangle = \frac{1}{R} \left(-\frac{\partial}{\partial s} \right)^q \tilde{R} \Big|_{s=0, k=0}, \quad (q = 1, 2, \dots), \quad (11)$$

$$\langle \rho^2 \rangle = \frac{-2}{R} \frac{\partial^2 \tilde{R}}{\partial k^2} \Big|_{s=0, k=0}. \quad (12)$$

3. A Diffusion-Based Framework for MSL Signal Prediction

[22] We still need a physically reasonable theory for $R(t, x, y) \equiv R(t, \rho)$ or, equivalently, $\tilde{R}(s, k)$ in order to use the above definitions and relations that predict the multiple-scattering cloud lidar signal and derived moments.

3.1. Simplified Transport Equations

[23] Now consider dense clouds, say, through which one cannot detect the silhouette and maybe not even the general direction of the sun in the transmitted radiance field. According to *Bohren et al.* [1995], this means optical thickness τ in excess of 8–10. We can safely assume that such light is transported via diffusion, the well-known approximation to RT per se. In other words, all is as if

photons detected in transmission or reflection were particles executing typically long convoluted random walks starting at the localized and collimated source and ending at a cloud boundary.

[24] A classic approach to diffusion theory (a.k.a. “P₁”) is to truncate the spherical harmonic expansion of the Green function radiance field at order one:

$$G(t, \mathbf{r}, \Omega) \approx [J(t, \mathbf{r}) + 3\Omega \cdot \mathbf{F}(t, \mathbf{r})]/4\pi \quad (13)$$

where we denote the zeroth- and first-order angular moments as

$$J(t, \mathbf{r}) = \int_{4\pi} G(t, \mathbf{r}, \Omega) d\Omega, \quad \mathbf{F}(t, \mathbf{r}) = \int_{4\pi} \Omega G(t, \mathbf{r}, \Omega) d\Omega, \quad (14)$$

respectively, the scalar (a.k.a. actinic) flux and vector flux. Accordingly, one assumes

$$p(\Omega \cdot \Omega') \approx [1 + 3g\Omega \cdot \Omega']/4\pi \quad (15)$$

for the phase function where g is the asymmetry factor (mean value of $\Omega \cdot \Omega'$). We note from the onset that (15) is a poor representation of the phase function of cloud droplets, most notably, the forward diffraction-induced peak is absent. By the same token, (13) is a poor representation of radiance anywhere near the highly collimated laser beam. We will treat these obvious problems separately further on, and thus improve the accuracy of the diffusion model in MSL.

[25] After substitution of (13) and (15) into (1), equations for this simplified transport theory are derived by angular integration term by term over 4π , once directly, and once after multiplication by Ω [*Case and Zweifel*, 1967]:

$$\frac{1}{c} \frac{\partial J}{\partial t} + \nabla \cdot \mathbf{F} = -\sigma_a(z)J + q_J(t, \mathbf{r}); \quad (16)$$

$$\frac{1}{c} \frac{\partial \mathbf{F}}{\partial t} + \nabla J/3 = -\sigma_t(z)\mathbf{F} + \mathbf{q}_F(t, \mathbf{r}). \quad (17)$$

In (17), a new and important coefficient appears: “transport” extinction,

$$\sigma_t(z) = (1 - g)\sigma_s(z) + \sigma_a(z) = (1 - \omega_0 g)\sigma(z), \quad (18)$$

where $\omega_0 = \sigma_s(z)/\sigma(z)$ is the previously introduced single-scattering albedo (assumed constant here). The transport MFP ℓ_t mentioned in the introductory section is given in terms of local variables by $1/\sigma_t(z)$. As in (14), we define

$$q_J(t, \mathbf{r}) = \int_{4\pi} Q(t, \mathbf{r}, \Omega) d\Omega, \quad \mathbf{q}_F(t, \mathbf{r}) = \int_{4\pi} \Omega Q(t, \mathbf{r}, \Omega) d\Omega. \quad (19)$$

[26] The “continuity” equation for radiant energy (16) is exact. Its counterpart for momentum in (17) is where the effect of the order-one truncation is felt, and it is further simplified by neglecting the time derivative. We thus obtain the “constitutive” equation:

$$\mathbf{F} = \frac{-1}{3\sigma_t(z)} \nabla J + \mathbf{q}_F(t, \mathbf{r})/\sigma_t(z), \quad (20)$$

a.k.a. Fick's law (especially when the last term is absent). This finalizes the local formulation of generic time-dependent 3-D diffusive transport theory.

[27] Photons produced by a doubled Nd:YAG laser, a staple of atmospheric lidar, have a wavelength of 532 nm at which water, condensed or not, has negligible absorption ($\sigma_a = 0$, $\sigma_s = \sigma$, $\varpi_0 = 1$) and, as previously mentioned, phase functions for observed droplet size distributions in warm boundary layer clouds yield $g \approx 0.85$ with remarkably small variability [Gerber *et al.*, 2000]. The continuity equation (16) thus becomes

$$\frac{1}{c} \frac{\partial J}{\partial t} + \nabla \cdot \mathbf{F} = q_J(t, \mathbf{r}), \quad (21)$$

a local expression of radiant energy conservation.

[28] For the MSL problem, when treated with separation of direct and diffuse components, (2) yields

$$\begin{aligned} q_J(t, \mathbf{r}) &= E_p \delta(x) \delta(y) \delta(t - z/c) \sigma_s(z) e^{-\int_0^z \sigma(z') dz'}, \\ \mathbf{q}_F(t, \mathbf{r}) &= q_J(t, \mathbf{r}) \times g \hat{\mathbf{z}}. \end{aligned} \quad (22)$$

3.2. Boundary Conditions

[29] If the cloud is reasonably stratiform and at least horizontally uniform, we can model it in slab geometry $\{\mathbf{r} \in \mathbb{R}^3; 0 < z < H\}$, and we recall that in this plane-parallel geometry cloud optical depth τ is the integral of $\sigma(z)$ from 0 to H . Expression of BCs for the above coupled PDEs for J and \mathbf{F} then call for hemispherical fluxes crossing a constant- z plane in the \pm directions, namely,

$$F_{\pm} = \int_{-\pi}^{+\pi} d\phi \int_0^{\pm 1} G(\cdot, \Omega) \mu d\mu = \frac{J/2 \pm F_z}{2}, \quad (23)$$

using (13). The “no incoming radiance” (a.k.a. “absorbing”) BCs for radiance bring us flux-based BCs

$$\begin{aligned} 4F_+(t, x, y, 0) &= J(t, x, y, 0) + 2F_z(t, x, y, 0) = 0, \\ 4F_-(t, x, y, H) &= J(t, x, y, H) - 2F_z(t, x, y, H) = 0, \end{aligned} \quad (24)$$

for all x , y , and t .

[30] Alternatively, but not equivalently in the present diffusion approximation, one can put the source in the BCs. In this case, we set $q_J = q_F \equiv 0$ in the RHS of (20)–(21) and require that

$$4F_+(t, x, y, 0) = J(t, x, y, 0) + 2F_z(t, x, y, 0) = 4q_0(t, x, y) \quad (25)$$

for a general distribution of isotropic sources at $z = 0$, in lieu of (24). The postulated boundary source $q_0(t, x, y)$ is the μ -weighted angular integral over $\mu > 0$ of the incoming radiance field at $z = 0$. In MSL, the radiance BC at $z = 0$ in (3) yields

$$q_0(t, x, y) = E_p \delta(x) \delta(y) \delta(t), \quad (26)$$

and the homogeneous BC at $z = H$ is unchanged. Note that, since flux alone tells us nothing about directionality, we are now effectively modeling the source as point-wise and pulsed but isotropic in the $\mu > 0$ hemisphere.

[31] Equations (24) and (25) express the least usual (third) type of BCs that occur in generic applications of diffusion-type PDE problems, both time-dependent (parabolic) or steady state (elliptical): they involve the density J at the boundary and the boundary crossing current F_z , equivalently, J and its normal derivative of J from (20). BCs can thus be expressed as a variable mixture of Dirichlet/first-type (fix J) and Neumann/second-type (fix F_z) BCs:

$$\begin{aligned} J(t, \vec{\rho}, 0) + 3\chi F_z(t, \vec{\rho}, 0) &= 4q_0(t, \vec{\rho}) \\ J(t, \vec{\rho}, 0) - 3\chi F_z(t, \vec{\rho}, H) &= 0. \end{aligned} \quad (27)$$

Although often referred to as “mixed” BCs, these are known technically as “Robin” BCs [Eriksson *et al.*, 1996]. At any rate, they are the most general BCs we will need to consider in MSL signal modeling.

[32] When $q_0(t, \vec{\rho})$ does not vanish, the BC mixing factor χ can differ from its $2/3$ value in (25), but typically not very much (at least in the most common transport applications). This is basically a tuning parameter that was introduced by early neutron transport theorists [e.g., Davison, 1958] to help diffusion theory reproduce high-precision solutions of the transport equations in critical applications; this boost in accuracy is naturally applied where diffusion is at its weakest, namely, boundaries. The physical interpretation of χ is that of an “extrapolation length” measured in transport MFPs. Indeed, in the absence of anisotropic internal sources, (20) tells us that $F_z(t, \vec{\rho}, 0) = -[\partial_z J / 3\sigma_t(z)]_{z=0}$, and similarly at $z = H$. By substitution into (27), the LHS reads as a linear extrapolation formula for J , given its derivative along the z axis, over a distance $\chi / \sigma_t(0)$ into the $z < 0$ region; we have a similar reading of the BC at $z = H$ going into the $z > H$ region.

3.3. Fields Observable With MSL

[33] The quantity of prime interest in MSL is local/instantaneous reflectivity, i.e., the outgoing flux normalized by total energy:

$$R(t, x, y) = \frac{F_-(t, x, y, 0)}{E_{\text{tot}}} = \frac{J(t, x, y, 0)/2 - F_z(t, x, y, 0)}{2E_{\text{tot}}} \quad (28)$$

where E_{tot} is the space-time integral of $q_J(t, \mathbf{r})$. Invoking the BC at $z = 0$ in (24), we can express this basic cloud response simply as

$$R(t, x, y) = \frac{J(t, x, y, 0)}{2E_{\text{tot}}}. \quad (29)$$

If the isotropic boundary source model in (27) is used for the BCs, then J and \mathbf{F} necessarily contain the incident flux. We must therefore compute the required space-time reflectivity field in (28) from

$$R(t, x, y) = \frac{F_-(t, x, y, 0)}{E_{\text{tot}}} = \frac{J(t, x, y, 0) - 2q_0(t, x, y)}{2E_{\text{tot}}} \quad (30)$$

where E_{tot} is defined as in (28) but for $q_0(t, x, y)$, hence without integrating over z .

[34] Finally, we recall that at cloud boundaries (and elsewhere) diffusion theory only predicts flux. A zeroth-order estimate of cloud-leaving radiance is given by $R(t, x, y)/\pi$, a Lambertian assumption which is not unreasonable for highly scattered light. A first-order angular model will use (13). This radiance-to-flux conversion can be done with better angular models, and should be for actual cloud remote sensing applications [cf. *Polonsky et al.*, 2005].

[35] Determination of the new lidar equation within the diffusion approximation, as formulated in the space-time domain, is now complete. Moreover, several options are available to control its degree of fidelity in source representation.

3.4. Formulation in Fourier-Laplace Space

[36] Fourier-Laplace transformation of the PDE system in (16) and (20), with BCs (24) or (25), leads to a class of analytically tractable problems for our representations of pulsed laser sources in the case of either constant coefficients, or simple enough variability models.

[37] Letting $\mathbf{r} = (x, y, z)^T = (\vec{\rho}, z)^T$, we define

$$\tilde{J}(s, \vec{k}; z) = \int_0^\infty dt \int_{-\infty}^{+\infty} \int_{-\infty}^{+\infty} \exp(-st + i\vec{k} \cdot \vec{\rho}) J(t, \vec{\rho}, z) d\vec{\rho}(x, y). \quad (31)$$

We similarly transform all the components of $\mathbf{F}(t, \vec{\rho}, z)$, yielding $\tilde{\mathbf{F}}(s, \vec{k}; z)$. We can now think of (s, \vec{k}) as parameters rather than independent variables, hence the “;” separator.

[38] Furthermore, let $\mathbf{F} = (\vec{F}_h, F_z)^T$, similarly for \mathbf{q}_F , and we recall that $\nabla = (\partial/\partial\vec{\rho}, \partial/\partial z)^T$ transforms to $(i\vec{k}, d/dz)^T$. Because of the axial symmetry of the source ($\vec{F}_h \equiv \vec{0}$), the (vector + scalar) PDE system in (20)–(21) reduces to two coupled 1D ODEs:

$$\tilde{J}'/3 = -\sigma_t(z)\tilde{F}_z + \tilde{q}_{F_z}, \quad (32)$$

$$\tilde{F}_z' = -\left(\frac{s}{c} + \frac{k^2}{3\sigma_t(z)} + \sigma_a(z)\right)\tilde{J} + \tilde{q}_J. \quad (33)$$

The latter ODE is an expression of energy conservation (with transport) along the z axis where local time variation and horizontal divergence of J are recast as “effective” absorption processes:

$$\sigma_a^{(e)}(s, k; z) = s/c + k^2/3\sigma_t(z). \quad (34)$$

This is a key coefficient that, in general, is stratified differently than $\sigma_x(z)$ ($x = s, a, t$), which all vary together (ω_0 and g being assumed constant).

[39] From (22), Fourier-Laplace transformed internal source terms used in MSL are

$$\tilde{q}_J(s, k) = E_p \sigma_s(z) e^{-(s/c)z - \int_0^z \sigma_a(z') dz'}, \quad \tilde{q}_{F_z}(s, k) = g \times \tilde{q}_J(s, k), \quad (35)$$

independent of k .

[40] The general BCs in (27) become

$$\tilde{J}(s, k; 0) + 3\chi \tilde{F}_z(s, k; 0) = 4\tilde{q}_0(s, k), \quad (36)$$

$$\tilde{J}(s, k; 0) - 3\chi \tilde{F}_z(s, k; H) = 0, \quad (37)$$

where $\tilde{q}_0(s, k) \equiv 0$ and $\chi = 2/3$ if the distributed internal source model in (35) is used. If the boundary point source model is used, $q_0(t, x, y)$ in (26) leads to $\tilde{q}_0(s, k) \equiv E_p$ in (36).

[41] We recall finally that, in multiple-scattering cloud lidar, our interest is limited to $\tilde{R}(s, k) = \tilde{J}(s, k; 0)/2E_p$ or, when using the boundary source option, $[\tilde{J}(s, k; 0) - 2\tilde{q}_0(s, k)]/2E_p$.

4. Laser Source as a Collimated Beam Decaying Exponentially Inside the Cloud

4.1. Forward Model for MSL Observables

[42] In this first application of the general diffusion framework, we start with the same assumptions as *Davis et al.* [1999] in their proof-of-concept paper on MSL observation of dense clouds: conservative scattering ($\sigma_a = 0$) and uniform cloud (constant $\sigma_s = \sigma$, and σ_t). However, rather than BCs with a source term, we use the more accurate representation of the pulsed laser beam formalized in (22), hence (35), as an exponential distribution of anisotropic internal sources. Assuming a unit pulse ($E_p = 1$), we must therefore solve

$$\begin{aligned} \tilde{F}_z' &= -\sigma_a^{(e)}(s, k)\tilde{J} + \sigma e^{-(s/c+\sigma)z}, \\ \tilde{J}'/3 &= -(1-g)\sigma\tilde{F}_z + g\sigma e^{-(s/c+\sigma)z}. \end{aligned} \quad (38)$$

Accordingly, we take $\tilde{q}_0(s, k) = 0$ in the general BCs (36)–(37) and set $\chi = 2/3$, leading to the Fourier-Laplace version of (24):

$$\tilde{J} + 2\tilde{F}_z|_{z=0} = 0, \quad \tilde{J} - 2\tilde{F}_z|_{z=H} = 0. \quad (39)$$

We anticipate dependence on both τ and on g , not just on $(1-g)\tau$. Also notice that s enters the exponential source term, as an effective σ_a , but $k^2/3\sigma_t$ does not. This transformed 3-D time-dependent problem is not formally identical to a solar two-stream problem, at least when $k \neq 0$.

[43] Following the steps described in the previous sections, we find at zeroth-order

$$R = 1 - T, \quad T = \frac{5 - e^{-\tau}}{3(1-g)\tau + 4}, \quad (40)$$

i.e., the well-known expressions for cloud albedo R and transmittance T for normal solar illumination and no absorption [*Meador and Weaver*, 1980]. Higher-order terms in k and s yield moments such as

$$\begin{aligned} \langle \rho^2 \rangle / H^2 &= \frac{20}{9} \frac{1}{(1-g)\tau} \times [1 + C_{\rho,2}(\tau, g)] \\ \langle ct \rangle / H &= \frac{5}{3} \times [1 + C_{ct,1}(\tau, g)] \\ \langle (ct)^2 \rangle / H^2 &= \frac{2}{3} (1-g)\tau \times [1 + C_{ct,2}(\tau, g)] \\ \langle (ct)^3 \rangle / H^3 &= \frac{4}{7} [(1-g)\tau]^2 \times [1 + C_{ct,3}(\tau, g)]. \end{aligned} \quad (41)$$

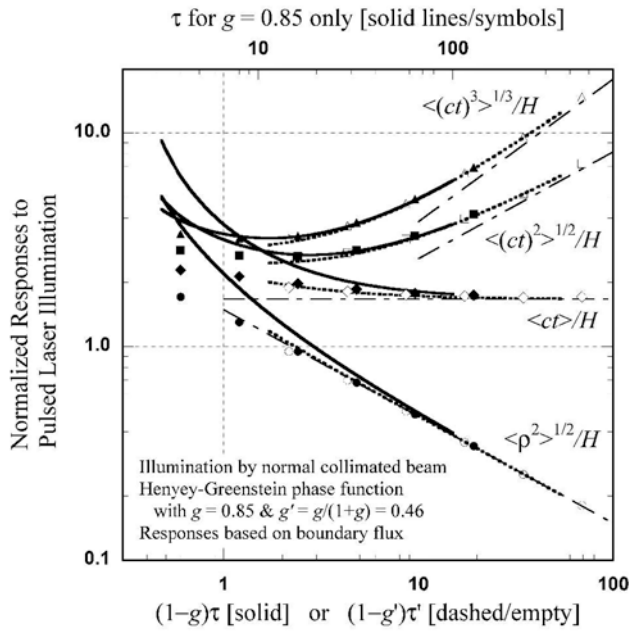


Figure 2. Four flux-based cloud responses from (41). Bottom to top on the RHS, we have $\sqrt{\langle \rho^2 \rangle}/H$, $\langle ct \rangle/H$, $\sqrt{\langle (ct)^2 \rangle}/H$, and $\sqrt[3]{\langle (ct)^3 \rangle}/H$, as functions of scaled optical depth $(1-g)\tau$ (bottom axis) with their corresponding asymptotes. The solid lines, for $g = 0.85$, are also given as functions of τ (top axis). The dashed lines are for $g' = g/(1+g) = 0.46$ versus rescaled optical depth $(1-g')\tau'$, on the bottom axis only. See main text for the use of the similarity relation $(1-g)\tau = (1-g')\tau'$, yielding $\tau' = \tau/3.6$ in this situation. Validation data for the forward diffusion-theoretical model are plotted with solid ($g = 0.85$) and open ($g' = 0.46$) symbols; they were obtained from MC simulations using 10^7 histories with Henyey-Greenstein scattering. All these cloud responses to laser illumination are obtainable from MSL, subject to a radiance-to-flux conversion with a reasonably good angular model.

Note that the temporal statistics are now expressed as moments of path ct in units of $[\text{length}]^q$. In the above relations, we also normalized all the moments with H^q ($q = 1, 2, 3$, as needed). Dependencies on cloud parameters on the RHS can thus be expressed only with dimensionless quantities: optical depth $\tau = \sigma H$ and g . In all cases, we give explicitly the dominant term for large τ and express the remainder as a multiplicative correction term that goes to unity (the C_s vanish) as $\tau \rightarrow \infty$. This representation emphasizes the fact that ratios of different moments (once expressed in the same physical units) are not constants, a remarkable property that is not found for transmitted light [Davis and Marshak, 2002]. This feature is of vital importance in MSL-based remote sensing and we can trace it to the characteristically balanced mixture of low and high orders of scattering in reflected light.

[44] It suffices here to say that the preasymptotic corrections $C_{\cdot,q}(\tau, g)$ have the form of rational functions of τ and g (also containing rapidly decaying terms in $e^{-\tau}$) that become increasingly complex as q increases. They all decay slowly in $1/\tau$ as $\tau \rightarrow \infty$. Complete expressions for the

above moments are supplied as auxiliary material¹ in the form of FORTRAN 77 code, and further details on their derivation are provided by A. B. Davis et al. (Space-time Green functions for diffusive radiation transport, in application to active and passive cloud probing, submitted to *Light Scattering Reviews*, 2008).

[45] As previously mentioned, a weakness of diffusion-based radiation transport modeling is the smooth one-parameter phase function in (15) whereas real-world phase functions have prominent forward peaks [Deirmendjian, 1969]. We can partially mitigate this disconnect by applying the classic δ -Eddington rescaling [Joseph et al., 1976]. The phase function is recast as a combination of a δ function in the forward direction (physically, just prolonged ballistic propagation) and a complementary term with two spherical harmonics. In the absence of absorption, this results in a rescaling given by

$$\sigma'(z) = (1-f)\sigma(z), \quad (1-g') = (1-g)/(1-f), \quad (42)$$

where f is the fraction of “ δ scattering.” This operation decreases $\sigma \equiv \sigma_s$ (increases the MFP), but leaves σ_t invariant in (18). It therefore has no effect on Davis et al.’s [1999] model since it depends only on $\tau_t = (1-g)\tau = \sigma_t H$.

[46] A popular choice is $f = g^2$ because it fits the spherical harmonic coefficients of the Henyey and Greenstein [1941] model phase function up to order 2, hence

$$g' = (g-f)/(1-f) = g/(1+g). \quad (43)$$

For liquid clouds, where $g \approx 0.85$, we get $\sigma' \approx 0.28\sigma$ and $g' \approx 0.46$.

[47] Figure 2 shows the dependence of the four normalized responses from (41) as functions of $(1-g)\tau = (1-g')\tau'$ when $g = 0.85$ and $g' = 0.46$ in log-log axes, using an RMS format for the second-order moments in space and time, and a $1/3$ power for the third-order moment in path. Figure 2 also demonstrates the validity of the updated diffusion model for its intended purpose (i.e., $(1-g)\tau \gtrsim 1$), and especially when using the rescaling based on g' in (43). This validation is based on a comparison of the diffusion-theoretical predictions in (41) with MC solutions of the more general RT problem in (1)–(2). We note that the preasymptotic corrections in (41) are clearly important, especially for the higher-order moments of path ct and/or when the g' rescaling is not used. Finally, the importance of using g' rescaling in diffusion theory is underscored by the violations of basic statistical inequalities (e.g., mean $>$ RMS) when $g = 0.85$ and $\tau \lesssim 10$.

4.2. Cloud Property Retrievals

[48] We note that cloud albedo and transmittance in (40) are available in lidar studies not only as the space/time integral of the MSL signal, but also from the solar or lunar background “signal” of well-calibrated lidar systems of any ilk, at least during daytime. After conversion from radiance to flux (or, better still, working with 1-D steady state radiance models) and accounting for the slant incidence

¹Auxiliary materials are available in the HTML. doi:10.1029/2007JD009666.

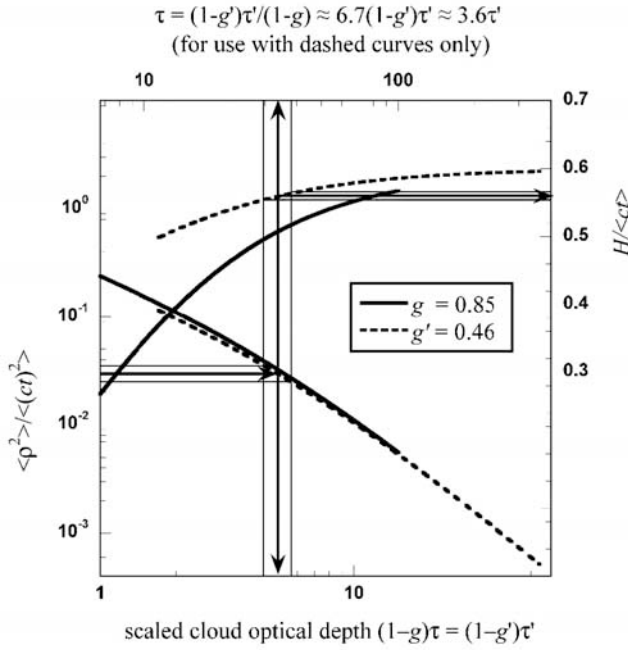


Figure 3. Typical moment-based cloud remote sensing algorithm with MSL. The bottom curves show the nondimensional ratio of observable moments $\langle \rho^2 \rangle / \langle (ct)^2 \rangle$ as a function of rescaled cloud optical depth $(1-g)\tau$ for $g = 0.85$ and the related value of $g' = 0.46$. Although not very different, one of these curves is chosen and gives us τ , optionally, via scaled optical depth τ' (top axis). We then use the corresponding prediction for $H/\langle ct \rangle$ in the top curves to determine cloud thickness H . The numerical example uses rescaled $g' = 0.46$ for a moment ratio of $(3.0 \pm 0.5) 10^{-2}$, yielding $\tau \approx 34 \pm 4$ (12% uncertainty) and $H \approx (0.560 \pm 0.005) \times$ the mean in-cloud path $\langle ct \rangle$. Note that the observational error on this first-order moment will very likely dominate the $\approx 1\%$ error on the multiplier (associated with $\approx 12\%$ on τ , resulting itself from $\approx 17\%$ on the second-order moment ratio).

angle, they can be used to retrieve τ . However, space-based and airborne instruments depending on R [Platt *et al.*, 1998; Yang *et al.*, 2008] will not be as sensitive as their ground-based counterparts that use T [Chiu *et al.*, 2007] when τ is large since $\partial \ln R / \partial \ln \tau \rightarrow 0$ while $|\partial \ln T / \partial \ln \tau| \rightarrow 1$ as $\tau \rightarrow \infty$.

[49] Only higher-order MSL observables however give us access to H and, furthermore, they can also deliver an estimate of τ , all of this without need for absolute calibration. From the cloud remote sensing perspective, we are glad to see that, starting with the asymptotic trends in (41), the four responses vary differently with τ . By obtaining from MSL observations any two of the four moments, we can therefore infer the two targeted cloud properties, namely, τ (given g) and then H .

[50] In Figure 3, we demonstrate the basic principle using the ratio $\langle \rho^2 \rangle / \langle (ct)^2 \rangle$, which is sensitive to scaled optical depth $(1-g)\tau$ but apparently almost completely insensitive to the specific choice of g itself (i.e., we can use either g or g' curves). Knowing τ (since we can safely prescribe g , hence g'), any one of the lidar moments will give us H by comparing the prediction in (41) and its observed counter-

part. In Figure 3, we propose to use $H/\langle ct \rangle$ which has the desirable property of being quite insensitive to τ , especially if we use g' rather than g . In this MSL cloud remote sensing demo, we have propagated graphically an assumed uncertainty of $\approx 17\%$ on the second-order moment ratio, leading to $\approx 13\%$ on τ and less than $\approx 1\%$ on the factor that converts $\langle ct \rangle$ to H .

[51] We have described here only moment-based retrieval methods in MSL observation of clouds. However, it is not always possible to estimate accurately the required moments from MSL data, say, due to an insufficiently large FOV resulting in a truncation of the observed Green function's tail. In Part 2, we revisit the direct PDF-based methodology of Polonsky *et al.* [2005] that overcomes this looming instrumental problem.

[52] What is the spatial resolution of an MSL-inferred cloud property? And what is the optimal spatial sampling? The answers of such questions usually involve the exposure time while the prevailing wind advects the cloud above a ground-based sensor, the transmitted beam divergence and platform velocity in airborne or satellite observations. It is remarkable that here the answers depend more on the cloud being observed. Indeed, by its very nature, the MSL signal originates from the whole volume of the cloud as defined by a horizontal area, say, a couple of times larger than $\pi \langle \rho^2 \rangle \dots$ which varies from cloud to cloud. We recall that the radius of that circular area is known as the “radiative smoothing scale” [Marshak *et al.*, 1995], and it defines the minimum pixel size at which passive cloud remote sensing can be performed without too much risk of contamination by adjacency effects. In MSL as well, any cloud structure smaller than this is smoothed by the radiative diffusion process. This smoothing scale also defines the minimum sampling distance (or time interval) that one would want to use in operational MSL observations. Anything faster would mean overlap in the radiative Green functions being measured, hence redundant cloud information. Anything slower will combine into a single observation the Green functions of cloud sectors that may have different physical properties; we are then faced with a nonlinear subresolution variability problem.

[53] If we absolutely had to set a specific value for the MSL “footprint” and the sampling scale, we would look at Figure 3 and note that $\sqrt{\langle \rho^2 \rangle}$ is on the order of H , which is typically $O(1)$ km and, generally speaking, is the least variable of the cloud parameters (at least within a given cloudy layer); at the same time, its dependence on τ is relatively weak (a fluctuation over an order of magnitude only yields a factor of ≈ 3). At any rate, MSL's inherent resolution is ideally suited for RT studies since smaller fluctuations affect only the bulk transport and call for a stochastic model (see below) while larger ones excite “adjacency” effects that call for a deterministic 3-D RT approach.

5. Impact of Internal Cloud Structure on MSL Observables

5.1. Stratification

[54] Stratiform clouds are expected to exhibit internal stratification. For instance, in their “convective cores,” liquid water content is predicted and widely observed

[Pawlowska *et al.*, 2000] to follow the adiabatic gradient, a linear trend in z over the vertical extent of the cloud. This classic result from the baseline parcel theory in cloud microphysics (number density assumed constant) leads to a $2/3$ power law in extinction from straightforward dimensional analysis. Formally, and depending on what side of the cloud is being illuminated by the laser source, we can write this as

$$\begin{aligned}\sigma_0(\gamma; z) &= \bar{\sigma} (1 + \gamma) (z/H)^\gamma, \text{ or} \\ \sigma_H(\gamma; z) &= \bar{\sigma} (1 + \gamma) (1 - z/H)^\gamma,\end{aligned}\quad (44)$$

with $\gamma \geq 0$ (in this case, $2/3$) and $\bar{\sigma}$ being the mean extinction (obtained, say, from cloud optical depth $\tau = \bar{\sigma}H$).

[55] This stratification in σ will directly affect the spatial (9) and temporal (8) observables in MSL, even if it does not affect the cloud's albedo in (7). Indeed, the local value of the MFP will be different at the top and bottom of the cloud and, physically, this means that the random walk representing the diffusing light propagation is scaled up (near cloud base) or down (near cloud top). Since MSL systems have already probed clouds from both sides, and will continue to do so, it is imperative to quantify the effect of stratification on the observables.

[56] Now, because g is assumed constant, $\sigma_t(z)$ will have the same behavior as $\sigma_{0,H}(\gamma; z)$. However, the vanishing $\sigma_t(z)$ at either $z = 0$ (lidar below cloud) or $z = H$ (lidar above cloud) is problematic for the diffusion model. Indeed, the BCs in (27) make necessary the evaluation of $F_z(t, \vec{p}, z)$ in (20) for $z = 0$ and $z = H$, one of which contains a division by $\sigma_t(z) = 0$. Physically, the local transport MFP is divergent and diffusion, as an approximation to RT, fails near one of the cloud boundaries (symptomatically, the associated extrapolation length is infinite).

[57] Instead of the troublesome power law model, we can take

$$\sigma_\Delta(z) = \bar{\sigma} \times [1 + \Delta (z/H - 1/2)] \quad (45)$$

where $|\Delta| < 2$ is the relative difference in extinction at the two cloud boundaries with respect to the mean, and similarly for $\sigma_{t,\Delta}(z)$ using $\bar{\sigma}_t = (1 - g)\bar{\sigma}$. The least-squares difference between the linear model in (45) and a given power law in (44) is minimized by the choice

$$\Delta(\gamma) = \pm 6 \times \left(2 \frac{\gamma + 1}{\gamma + 2} - 1 \right) \quad (46)$$

where $+$ is mapped to $\sigma_0(\gamma; z)$ and $-$ to $\sigma_H(\gamma; z)$. Values of special interest are $\Delta = \pm 3/2$ since they approximate $\gamma = 2/3$, the above-mentioned expectations based on parcel theory for a cloud illuminated from below and above respectively.

[58] Ideally, we would like to extend the new collimated/anisotropic internal source model to the case of internal variability. However, the resulting ODE problem does not appear to be analytically tractable. We therefore revert to the isotropic boundary point source model used by Davis *et al.* [1999]. We thus wish to solve both the space domain ($s = 0$) problem of MSL,

$$\tilde{F}' = -[k^2/3\sigma_{t,\Delta}(z)]\tilde{J}, \quad \tilde{J}' = -3\sigma_{t,\Delta}(z)\tilde{F}, \quad (47)$$

and its time domain ($k = 0$) counterpart,

$$\tilde{F}' = -(s/c)\tilde{J}, \quad \tilde{J}' = -3\sigma_{t,\Delta}(z)\tilde{F}, \quad (48)$$

in both cases, subject to

$$\tilde{J} - 3\chi\tilde{F}_z|_{z=0} = 4, \quad \tilde{J} + 3\chi\tilde{F}_z|_{z=H} = 0, \quad (49)$$

leaving χ as an unspecified parameter. By inspection, we see that nondimensional cloud responses can only depend on Δ and $\tau_t = \bar{\sigma}_t H$ (and χ). In contrast with the $\Delta = 0$ [Davis *et al.*, 1999; Love *et al.*, 2001a], we will not have similar behavior between s/c and $k^2/3\sigma_t$ since they are interchangeable in $\sigma_a^{(e)}(s, k)$ only when $\Delta = 0$.

[59] Spatial and temporal moments are computed as previously: (1) solve boundary value problem for coupled ODEs; (2) obtain $\tilde{R}(s, 0)$ from $\tilde{J}(s, 0; z = 0)$, or $\tilde{R}(0, k)$ from $\tilde{J}(0, k; z = 0)$; (3) expand into a Taylor series of the desired length in the variable of interest and extract the moments of interest; and (4) translate result into a high-level programming language for easy manipulation and plotting. A computer-assisted algebra tool is highly recommended for all of the above steps.

[60] As it turns out, the Fourier domain (spatial) diffusion problem in (47) and (49) for $\tilde{J}(0, k; z)$ is solvable in terms of order-zero and order-one modified Bessel functions of the first and second kinds. The Laplace domain (temporal) diffusion problem in (48) and (49) for $\tilde{J}(s, 0; z)$ is solvable in terms of Airy functions and their derivatives, which are related to modified Bessel functions with $1/3$ -integer orders. At zeroth order, we retrieve (using L'Hôpital's rule)

$$R = 1 - T, \quad T = \frac{1}{1 + \tau_t/2\chi}, \quad (50)$$

the well-known [Schuster, 1905; Meador and Weaver, 1980] expression for cloud transmittance T for diffuse illumination in the absence of absorption, and cloud albedo R . As expected, they are not sensitive to internal structure since optical properties ϖ_0 and g are held constant. For MSL observables proper, higher-order terms in k and s yield

$$\begin{aligned}\langle \rho^2 \rangle / H^2 &= \chi \frac{(2 + \Delta)^4 \ln[(2 + \Delta)/(2 - \Delta)] - 4\Delta(4 + \Delta(8 + \Delta))}{8\Delta^3} \frac{1}{\tau_t} \times \dots, \\ \langle ct \rangle / H &= \chi \frac{40 + \Delta(10 + \Delta)}{20} \times \dots, \\ \langle (ct)^2 \rangle / H^2 &= \chi \frac{320 + \Delta(80 - \Delta(20 + \Delta(10 + \Delta)))}{400} \tau_t \times \dots,\end{aligned}\quad (51)$$

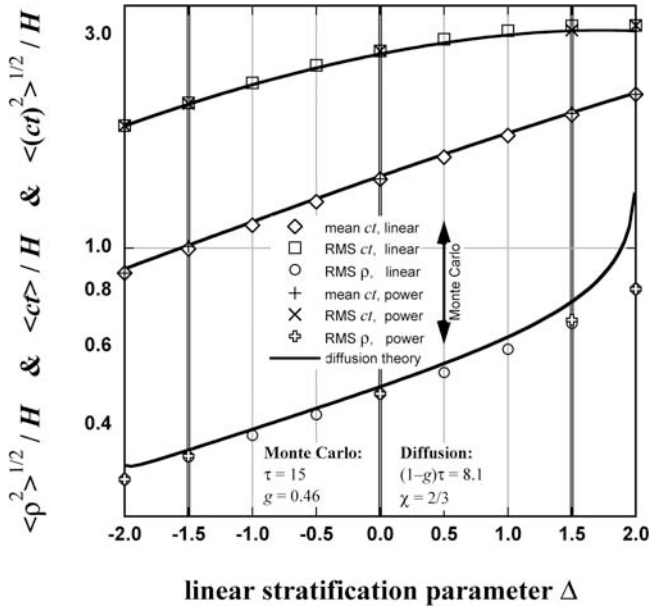


Figure 4. Modeling stratification inside plane-parallel clouds. The solid lines are the diffusion predictions for the three moments in (51), normalized to $H = 1$, plotted against the relative gradient parameter $\Delta = [\sigma(z = H) - \sigma(z = 0)]/\bar{\sigma}$ where $z = 0$ defines the illuminated/observed cloud boundary. Since extinction generally increases with altitude, $\Delta > 0$ applies to ground-based MSL while $\Delta < 0$ applies space-based MSL (or airborne, from above the cloud deck). The assumed cloud has $\tau_t = (1 - g)\tau = 8.1$. The source term for the ODE problem is expressed in the BCs, which use $\chi = 2/3$. Open symbols are from nine MC runs over the range of Δ at 0.5 increments, each using $2 \cdot 10^7$ histories with $g = 0.46$ Henyey-Greenstein scattering. All of this is for the linear-trend model in (45). Crosses are for the more attractive power law models in (44) with $\gamma = 2/3$, using the least-squares connection in (46) to position them on the $\pm\Delta$ axes, namely, $\gamma(\Delta) = 2|\Delta|/(6 - |\Delta|)$. There is hardly any difference in any moment for the nontrivial cases at $\Delta = \pm 3/2$.

where we have to envision the preasymptotic correction terms in $1 + C_{\cdot q}(\tau_t/2\chi, \Delta)$. Davis et al. (submitted manuscript, 2008) provide further details on the derivation of these expressions, while FORTRAN 77 code for computing them can be found in the auxiliary material. All the prefactors we have highlighted here revert to those by Love et al. [2001a], equations (9)–(11) when $\Delta \rightarrow 0$.

[61] Figure 4 illustrates the outcome of the above diffusion-based models. We examine specifically the case $\tau_t = 8.1$ (e.g., $\tau = 54$ when $g = 0.85$) and set $\chi = 2/3$. Results from MC simulations for linearly stratified clouds with $\tau = 15$ are also plotted for validation purposes, hence using an isotropic boundary point source and the Henyey-Greenstein phase function with $g = 0.46$. Two MC simulations were also run using the “ $\gamma = 2/3$ ” power law model for $\sigma(z)$ starting at $z = 0$ (mapped to $\Delta = +3/2$) and $z = H$ (corresponding to $\Delta = -3/2$). There is hardly any difference in these MC predictions for all three moments, and we already know there is none at all for $\gamma = 0$ and 1 (related respectively to $\Delta = 0, \pm 2$).

[62] Overall, the diffusion results are just slightly offset from their MC counterparts. The most remarkable difference between diffusion and MC is the logarithmic divergence of $\langle \rho^2 \rangle$ at $\Delta \rightarrow 2^-$ that is manifest in (51). All is as if the effective diffusivity constant $\langle \rho^2 \rangle / \langle t \rangle$, as observed by MSL at the cloud boundary, becomes infinite with the value of the transport MFP at $z = 0$, namely, $\ell_t(0) = 1/\bar{\sigma}_t(1 - \Delta/2)$. As stated above, diverging ℓ_t is clearly a challenge for the diffusion model since trajectories become ballistic, and apparently more so when this occurs near the source. This problem could probably be fixed by introducing a parameterization $\chi(\Delta)$ where $\chi \rightarrow 0$ as $\Delta \rightarrow 2^-$.

[63] We also note in the log-lin plot that the MC results for $\langle ct \rangle$ and $\langle \rho^2 \rangle^{1/2}$ are quasi-linear in Δ over its full range. This is especially good for spatially resolved MSL observations from ground ($\Delta > 0$) since, instead of the diffusion model per se, one can use a log-linear extrapolation from the log sensitivity of these moments to Δ evaluated at $\Delta = 0$. Specifically, we propose to use

$$\frac{\partial}{\partial \Delta} \ln \sqrt{\langle \rho^2 \rangle} \Big|_{\Delta=0} = \frac{\partial}{\partial \Delta} \ln \langle ct \rangle \Big|_{\Delta=0} = \frac{X(1+X)}{3+6X+4X^2}, \quad (52)$$

where $X = \tau_t/2\chi$, as a simple way of capturing the effect of stratification. For $\langle (ct)^2 \rangle$ however, it is best to use the detailed expression from the auxiliary material. In all cases, one can use the required moment value at $\Delta = 0$ from a more accurate model (e.g., from the previous section), or even a tabulated MC result; that hybrid approach should further reduce any bias.

5.2. Random Variability

[64] Barker and Davis [2005] showed that there are two broad classes of models in 3-D RT that go after the large-scale effects of unresolved small-scale variability in cloud structure, which is invariably assumed random. Members of one class of mean field theory end with new transport equations to solve. Members of the other class pursue homogenization: redefine coefficients in 1-D RT so that the known solutions of that problem capture the main 3-D effects, which is clearly the path of least resistance. Among these “effective medium” approaches to random 3-D variability, we favor the rescaling technique by Cairns et al. [2000]. Although it is a one-parameter solution, it stems from a careful renormalization treatment of both one- and two-point statistics, i.e., the PDF of $\sigma(\mathbf{r})$ and its autocorrelation function respectively.

[65] Starting with the δ -rescaled (primed) quantities in (42) that account for problematic forward scattering peaks, we have:

$$\sigma''(z) = (1 - \epsilon)\sigma'(z), \quad (1 - g'') = (1 - g')[1 - \epsilon/(1 - \epsilon)], \quad (53)$$

in the case of conservative scattering, where ϵ is the variability parameter. While δ rescaling leaves the product $(1 - g)\sigma$ invariant, it decreases here both through σ and through $1 - g$ as ϵ increases (since $g'' > g'$).

[66] Letting overscores denote averages over the spatial disorder, Cairns et al. show specifically that for moderate-amplitude 3-D effects one has

$$\epsilon = a - \sqrt{a^2 - V} \quad (54)$$

Table 1. Properties of a Cloud With $H = 0.5$ km Probed by MSL From Both Sides in Table 2

Quantity	Symbol	Unit	Given	δ -Scaled	Cairns-3D	Above	Below
Parameter of interest			Δ	f	ϵ	Δ	Δ
Parameter value		[–]	0	0.72	0.15	–1.5	+1.5
<i>Cloud Optical Properties</i>							
Optical depth	τ	[–]	25	6.94	5.89		
Asymmetry factor	g	[–]	0.85	0.46	0.56		
Scaled optical depth	$(1 - g)\tau$	[–]	3.75	3.75	2.62		
<i>Cloud Radiative Responses</i>							
Albedo	R	[–]	0.67	0.67	0.58		
Mean in-cloud path	$\langle ct \rangle$	km	1.04	0.91	0.99	0.74	1.32
RMS lateral transfer	$\sqrt{\langle \rho^2 \rangle}$	km	0.30	0.28	0.34	0.26	0.46
Average MSL radiance	equation (55)	$\frac{\text{photon}}{\text{s} \cdot \text{m}^2 \cdot \text{sr} \cdot (\text{laser photon})}$	0.22	0.29	0.15	0.36	0.063

where $V = \overline{\sigma^2}/\bar{\sigma}^2 - 1$ (variance relative to mean-squared) and $2a = 1 + 1/\bar{\sigma}l_c$. We denote here the characteristic correlation scale of the spatial variability by l_c . We see that small-scale fluctuations, i.e., when $l_c \ll \text{MFP} \approx 1/\bar{\sigma}$, have little effect since $\epsilon \approx 2V/(2a)^2 \ll 1$ (irrespective of V) as a becomes very large. Large-scale fluctuations ($\bar{\sigma}l_c \gtrsim 1$) can have a strong impact ($\epsilon \lesssim 1$); however, this stretches the validity of the model (in particular, amplitude is then limited to cases where $V \leq a^2 \lesssim 1$). For very large-scale fluctuations ($\bar{\sigma}l_c \gg 1$, hence $a \approx 1/2$, hence $V \lesssim 1/4$), it is clear that one should average over macroscopic MSL responses rather than try to find an effective medium to account for variability effects in the spirit of an Independent Pixel Approximation [e.g.] [and references therein *Barker and Davis*, 2005]. That is precisely how *Davis and Marshak* [2002] approached the problem of spatial variability: following *Barker* [1996], they averaged expressions similar to those in (41), but for transmission, over a Gamma distribution of σ values.

[67] The above scale-by-scale breakdown of spatial variability impacts is consistent with the first-principles analysis by *Davis and Marshak* [2004] who, incidentally, show that the actual MFP is $1/\bar{\sigma}$ in a broad class in variable media, and this always exceeds $1/\bar{\sigma}$ (they are equal only when σ is uniform).

6. Signals and Noises in Multiple-Scattering Cloud Lidar

6.1. Signal-to-Noise Ratio Estimation

[68] Before we consider the use of MSL data for cloud remote sensing purposes, it is standard procedure to evaluate the typical signal as realistically possible given the specifications of actual or proposed instruments. At the same time it is important to quantify all foreseeable sources of noise and, from there, estimate a priori the signal-to-noise ratio (SNR). The main purposes of such exercises are to test ideas in instrument design as well as to experiment with different sampling strategies for observations, in this case, of different types of cloud.

[69] We now illustrate this key modeling application of the above theoretical results for MSL observables. In this demonstration, we will focus on two specific MSL systems that probe clouds from either side:

[70] 1. The Wide-Angle Imaging Lidar (WAIL) is a ground-based design developed at Los Alamos National

Laboratory. It has already been deployed several times in New Mexico [*Love et al.*, 2001a, 2001b] and once in Oklahoma [*Polonsky et al.*, 2005]. Yet the current engineering model is still being refined and we will use here parameters for so-far untested hardware.

[71] 2. The Lidar-in-space Technology Experiment (LITE) was the first demonstration of space-based lidar conducted, largely from NASA’s Langley Research Center, as a payload in the cargo bay of Space Shuttle Discovery during flight STS-64 [*Winker et al.*, 1996]. This mission was flown 9–20 September 1994, and was considered a vast success that indeed blazed the path for current and future lidar satellite missions, including NASA’s ICESat/GLAS and CALIPSO/CALIP.

[72] We use the same cloud in both cases: a typical boundary layer stratus deck at 0.7 km altitude, with $H = 0.5$ km, $\tau = 25$, and $g = 0.85$. Table 1 summarizes all the intermediate time-dependent 3-D RT modeling results leading to the temporally, spatially and angularly averaged radiance excited by the pulsed laser illumination that escapes the illuminated/observed cloud boundary. We estimate this basic quantity from

$$I_{\text{obs}} \approx \frac{R/\pi}{\pi \langle \rho^2 \rangle \langle t \rangle}, \quad (55)$$

and it will be expressed in its natural radiometric units, namely, photons per laser photon, per unit of aperture area, per steradian of FOV, and per unit of exposure time. At sufficient accuracy, this is also the radiance detected across (essentially empty) space by the MSL receiver.

[73] Standoff distances d_{obs} are of course very different: 0.7 km for WAIL, ≈ 259 km for LITE. The next question is what solid angle and viewing angle are subtended by the $\approx \pi \langle \rho^2 \rangle$ circular area of the observed radiative Green function. This “adapted” solid angle is given by

$$\delta\Omega_{\text{Gf}}(d_{\text{obs}}) = \frac{2\pi}{d_{\text{obs}}^2/\langle \rho^2 \rangle + 1} = 2\pi(1 - \cos \theta_{\text{Gf}}). \quad (56)$$

The corresponding adapted viewing angle $\theta_{\text{Gf}}(d_{\text{obs}})$ is 45.5° for WAIL and 0.06° (≈ 1 mrad) for LITE. Ideally, one wants the MSL instrument’s FOV ($2 \times \theta_{\text{max}}$) to be at least this large, and not too much more. Say, $\tan \theta_{\text{max}} \approx 2$ to 3 times

Table 2. Specifications for Two MSL Systems and Expected SNRs

Quantity	Symbol	Unit	LITE	WAIL
Standoff distance	d_{obs}	km	259	0.7
Equation (56)	$\delta\Omega_{\text{Gr}}$	sr	$4 \cdot 10^{-6}$	1.8
“Adapted” FOV ^a	$2\theta_{\text{Gr}}$	deg	0.06	91
<i>Transmitter Parameters</i>				
Wavelength	λ	nm	532	532
Power = $E_p \times \text{RepRate}$	P	W	5	5
Pulse frequency	RepRate	Hz	10	$12 \cdot 10^3$
Pulse energy	E_p	mJ	500	0.42
Photons per pulse	$E_p \lambda / hc$	[–]	$1.34 \cdot 10^{18}$	$1.12 \cdot 10^{15}$
<i>Receiver Parameters</i>				
Optical throughput	OTp	%	45 ^b	70
Quantum efficiency	η_λ	%	14	70
Aperture area (effective)	A	m ²	0.63	10^{-5}
FOV (full width) ^a	$2\theta_{\text{max}}$	deg	0.20	88
$\delta\Omega_{\text{FOV}}/\text{U1R_to_F}$	$\frac{2(1-\cos\theta_{\text{max}})}{(1-\cos 2\theta_{\text{max}})/2}$	[–]	$1 + 3 \cdot 10^{-6}$	1.163
Étendue	$A \times \text{U1R_to_F}$	m ² · sr	$6 \cdot 10^{-6}$	$15.5 \cdot 10^{-6}$
Filter bandpass	$\Delta\lambda$	nm	0.35	50
<i>Sampling and Averaging</i>				
Path bin size	δct	m	10	10
Integration time	Δt	s	0.1	300
Number of pulses	N_p	[–]	1	$3.6 \cdot 10^{6c}$
<i>Predictions</i>				
Signal	$S_{\delta ct}(\Delta t)$	counts	2721 ^b	$341 \cdot 10^3$
Only shot noise	$\text{SNR}_{\text{night}}$	[–]	78	584
+ lunar background	$\text{SNR}_{\text{l-moon}}$	[–]	38	19
+ solar background	$\text{SNR}_{\text{daytime}}$	[–]	$4.3 \cdot 10^{-2}$	$2.6 \cdot 10^{-2}$

^aThis happens to be slightly more (WAIL) or, as recommended in the main text, somewhat smaller (LITE) than the actual FOV $2\theta_{\text{FOV}}$.

^bNighttime value for LITE; daytime value is 20%, which affects equally signal and background, hence an SNR decrease by $\sqrt{20/45} \approx 0.67$ accounted for in the tabulated value in the last row.

^cAs explained in text, this pulse budget is distributed equally among path bins; assuming 272 bins, $N_p = 3.6 \cdot 10^6/272 \approx 13.2 \cdot 10^3/\text{bin}$ (an integration over 1.1 s per bin).

$\langle \rho^2 \rangle^{1/2}/d_{\text{obs}}$. Indeed, the observed radiance field is concentrated in this region of direction space. As it turns out, LITE satisfies this constraint and WAIL almost does. If that were not the case, θ_{max} too small means loss of signal while too big adds little signal in view of its exponential decay in space (only more background noise is collected).

[74] Table 2 lists the relevant transmitter and receiver parameters for LITE (as flown) and WAIL (new/untested configuration). To illustrate SNR estimation we focus on the temporal aspect of MSL, which is the only one LITE could access in detail. We therefore seek an expression for the number of “photon counts” $S_{\delta ct}(\Delta t)$ registered in a typical path length bin of size δct when integrating MSL signal over all of space but only a given time interval Δt . For the average time-dependent radiance in (55), basic radiometry gives us

$$\begin{aligned}
 S_{\delta ct}(\Delta t) &\approx \text{OTp} \times \eta_\lambda \\
 &\times \left(\frac{E_p}{hc/\lambda} \times I_{\text{obs}} \right) \\
 &\times (A \times \text{U1R_to_F}) \times \delta ct \\
 &\times (\text{RepRate} \times \Delta t)
 \end{aligned} \tag{57}$$

in photon counts, where $\text{U1R_to_F} = \pi \sin^2 \theta_{\text{max}} = \pi(1 - \cos 2\theta_{\text{max}})/2$ is the proper conversion-to-flux factor for a uniform distribution in direction space of unitary radiance. This quantity is used in lieu of the usual expression $\delta\Omega_{\text{FOV}} = 2\pi(1 - \cos \theta_{\text{max}})$, a somewhat larger value (see Table 2). This substitution is necessary in MSL studies because the FOV can be very large indeed. The last term in parentheses is just the total number of pulses used. Other new symbols are defined in Table 2 where values for LITE and WAIL are listed. In particular, we note that étendue ($A \times \text{U1R_to_F}$), which appears in (57), is commensurate in both systems in spite of their huge difference in bulk (as measured, say, by aperture area A).

[75] Next, we estimate the noise level in the same units (photon counts). For an ideal MSL system operating on a moonless night, the only source of noise is the inherent Poisson randomness of photon arrivals, a.k.a. “shot” noise; its RMS value is simply $\sqrt{S_{\delta ct}(\Delta t)}$. Real optical instruments of course have an irreducible source of noise, a.k.a. “dark current” (fluctuations), from its electronics that is present even when there is no light. We will not concern ourselves with it here beyond this mention; it should be the smallest component anyway. The third and last source of noise is the steady ambient light, i.e., the solar or lunar background. In view of its Poissonian nature, its mean and/or variance is estimated (in counts) from

$$\begin{aligned}
 \text{BG}(\Delta t) &\approx \text{OTp} \times \eta_\lambda \\
 &\times \left(T_{\text{dif}}(\mu_0) \times \frac{\mu_0 F_{0\lambda}/\pi}{hc/\lambda} \right) \\
 &\times (A \times \text{U1R_to_F}) \\
 &\times (\Delta t \times \Delta\lambda),
 \end{aligned} \tag{58}$$

where $\Delta\lambda$ is the width of the background suppression filter (see Table 2), μ_0 is the cosine of the solar/lunar zenith angle, $T_{\text{dif}}(\mu_0)$ is cloud’s diffuse transmittivity to the ground (but we use the cloud’s reflectivity $R(\mu_0)$ if the MSL is above it), and $F_{0\lambda}$ is the solar/lunar spectral flux incident on the top of the atmosphere. For the solar background, we have $F_{0\lambda} = 1.869 \text{ W/m}^2/\text{nm}$ at $\lambda = 532 \text{ nm}$ [American Society for Testing and Materials, 2000]. For the nighttime counterpart, the Moon is assumed to be a Lambertian reflector (albedo 0.12) subtending $32'$ of arc (solid angle modulated by phase angle) receiving the same irradiation.

[76] Being three independent sources of noise, their variances are additive, and total RMS noise amplitude is

$$N_{\delta ct}(\Delta t) \approx \sqrt{S_{\delta ct}(\Delta t) + \text{BG}(\Delta t) + \text{electronics}}, \tag{59}$$

where the last term is to be expressed in “equivalent counts.”

[77] The last subtlety to consider in MSL time domain SNR estimation is that WAIL’s current detector (an intensified/gated CCD camera) visits each time/path bin sequentially to cumulate signal. In contrast, LITE (as most other lidars) acquire signal for all its time bins at once. This means that for WAIL the total number of laser pulses ($\text{RepRate} \times \Delta t$) in the overall integration time must be divided among a relatively large number of separate bins.

We will assume that there are just enough bins, each δt wide, to cover $3 \times t^*$ where

$$t^* = (H/c) \times \frac{(1-g)\tau}{3(\pi R)^2}, \quad (60)$$

is the exponential decay rate of the Green function in time [Polonsky and Davis, 2004, or Part 2], with R being obtained from $(1-g)\tau$ in (50) with $\chi = 2/3$. For the cloud of present interest, we find $ct \approx 0.85$ km in units of path. This rationale leads to 272 time bins, and Δt is set to 5 min (300 s, 3.6×10^6 pulses), which is basically enough for ~ 1.5 km of cloud to advect by at nominal wind speeds (~ 5 m/s). This is not far from optimal since any faster sampling of the radiative Green function would have overlap due to the horizontal transport. In contrast, LITE is moving along its orbit at 7 km/s. In this case, we want to get signal from every pulse, hence $\Delta t = 1/\text{RepRate} = 0.1$ s.

6.2. Discussion

[78] The last three rows of Table 2 give

$$\text{SNR} = S_{\delta ct}(\Delta t) / N_{\delta ct}(\Delta t) \quad (61)$$

for the two MSL systems (neglecting electronic noise) under three scenarios: moonless night, moon present, and daytime.

[79] In the last two situations, we need to compute $F = T_{\text{diff}} R$, for which it suffices to use predictions from two-stream theory [Meador and Weaver, 1980] for the given cloud (after δ -Eddington and Cairns rescalings). We take $\mu_0 = 0.5$ for WAIL and $\cos 51^\circ$ for LITE. This last value is for the actual zenith angle of the moon at 6:53 GMT on 9/16/94 viewed from 36°N by 128.6°W , which is approximately when and where the LITE data analyzed in Part 2 was captured during nighttime orbit # 135 (the moon was 87% full). For WAIL, we assume an average solar/lunar zenith angle (and, worst case scenario, a full lunar disk).

[80] We conclude from these SNR estimates that the two radically different MSL systems have and will perform well at night, even with a full moon. However, daytime operation remains a challenge: the SNR must be boosted by at least $\sim 10^3$, and increasing Δt by 10^6 is clearly not an option. Current plans at LANL for the WAIL project [Love et al., 2001b] involve an ultranarrow ($\Delta\lambda \approx 5$ pm) magneto-optic (a.k.a. Faraday) filter centered on one of the sodium lines in its strong doublet near 589 nm, where the sun ($F_{0\lambda}$) is already about $20\times$ dimmer than at nearby wavelengths. Contrary to interference-based monochromators, such filters have a very wide acceptance angle, which is critical to the present application. Even factoring in that $\lambda F_{0\lambda}$ is somewhat larger at 589 nm than at 532 nm, we are close to our goal. However, a sufficiently stable and powerful tunable laser is required to utilize this sophisticated background rejection technique.

[81] Another approach altogether is to complement operational MSL systems with high-resolution oxygen A-band spectrometers, a passive technique in the solar spectrum. The main products of these instruments for cloudy skies are indeed the successive moments of path length [Pfeilsticker et al., 1998; Min and Harrison, 1999], i.e., $\langle (ct)^q \rangle$, $q = 1, 2, 3$

(maybe more). All time-only cloud MSL remote sensing techniques are therefore amenable to these data. It is important to keep this in mind when NASA launches in late 2008 the first high-resolution oxygen A-band spectrometer into space on the Orbiting Carbon Observatory (OCO) mission [Crisp et al., 2004].

7. Summary

[82] We have considerably refined the diffusion-theoretic forward model for predicting space-time signals from multiple-scattering cloud lidar. More precisely, we targeted moments of the observable space-time Green function as expressions of the cloud's physical thickness H and optical depth τ (considered as the remote sensing unknowns), and the asymmetry factor g of the scattering phase function. In the original model by [Davis et al., 1999], moments (normalized by H) were only functions of scaled optical depth $(1-g)\tau$. We have added to that capability (1) accurate representation of the pulsed laser source as a collimated anisotropic exponentially decaying spatial distribution of internal sources, and consequently separation of the (smooth) scattered and (singular) uncollided components of radiance; (2) δ -Eddington rescaling (that preserves $(1-g)\tau$) further improves the above refinement by partially accounting for the strong forward scattering peak in the phase functions of observed cloud droplet populations (since normalized moments are now functions of τ and g); (3) parameterization of the impacts of internal cloud stratification using an analytically tractable model to compute the sensitivity of moments to a constant gradient in extinction $\sigma(z) \propto 1 + \Delta \times (z/H - 1/2)$; (4) use of the above linear gradient model to mimic the more relevant case of power law behavior, as an important instance, extinction increasing as a $2/3$ power from cloud base is mapped to $\Delta = 2[\sigma(H) - \sigma(0)]/[\sigma(H) + \sigma(0)] = \pm 3/2$; and (5) Cairns et al. [2000] rescaling that changes τ and g (without conserving $(1-g)\tau$), which defines an effective optical medium that captures the systematic effects on space-time cloud responses of turbulence-driven random internal variability at scales up to a few mean free paths. All but the last item received at least limited validation by comparison with Monte Carlo simulations. Items 3–4 are critically important as one switches between illumination/observation of the cloud from below (ground-based probes) and from above (airborne or space-based systems).

[83] This effort brings the diffusion modeling project to a state of balance between formal sophistication and practical utility. The main drivers for this development are (1) physical insights gained from a PDE-based approach, (2) accuracy sufficient for applications in instrument and/or algorithm design, (3) flexibility in the representation of cloud structure as well as of radiation sources and sinks, and (4) extreme computational efficiency of analytical methods that enables real-time data processing when and where multiple-scattering cloud lidars will be deployed operationally on ground or in space.

[84] As an example of activity in algorithm design, the refined model's features are showcased with a demonstration of how H and τ , hence extinction $\sigma = \tau/H$, can be derived from multiple-scattering cloud lidar data of sufficient quantity and quality to estimate selected moments

reliably. The retrieved cloud properties are representative of large-volume averages, on the order of $H^3/(1 - g)\tau$.

[85] As an example of activity in instrument design, the improved diffusion model is applied to signal-to-noise ratio (SNR) estimations for two very different multiple-scattering lidar systems. SNR is computed a priori for a new, so far untested, configuration of LANL's Wide-Angle Imaging Lidar (WAIL); it is also computed a posteriori for NASA's Lidar-In-space Technology Experiment (LITE). Part 2 of this series (Davis et al., manuscript in preparation, 2008) will demonstrate innovative ways of extracting cloud properties from real data collected with these two systems, and compare their outcome with available cloud information from other sources.

[86] If even more realistic representations of the scattering phase function and/or 3-D cloud structure are needed in the applications, without paying too high a price in CPU cycles, then one should turn to ultraefficient numerical techniques. For instance, data exploitation in the two airborne multiple-scattering cloud lidar systems in existence use (1) a neural network trained with one-time 3-D Monte Carlo runs [Evans et al., 2003, 2006] and (2) a multidimensional look-up table populated with one-time 1-D Monte Carlo runs [Cahalan et al., 2005]. Another promising approach, which is more closely related to the present diffusion model, would use the rapid numerical time-dependent two-stream solver developed recently by Hogan and Battaglia [2008]. In particular, its representation of the pulsed laser source uses a small-angle multiple forward scattering model by Hogan [2008] that is of practical interest in its own right for processing (on- or near-beam) lidar data from optically thin clouds and optically thick aerosol layers. Although designed for probing dense clouds, deployed multiple-scattering lidar systems will continue to collect data under such semiclear skies. It will be interesting to see what added value they can contribute to aerosol and cirrus studies.

[87] **Acknowledgments.** The authors are grateful for financial support from the U.S. DOE Atmospheric Radiation Measurement (ARM), project SCFY041020, and from LANL's Laboratory-Directed R&D (LDRD) programs. We thank Luc Bissonnette, Bob Cahalan, Frank Evans, Robin Hogan, Steve Love, Matt McGill, Alexander Marshak, Igor Polonsky, James Spinhirne, Tamas Várnai, Dave Winker, Warren Wiscombe, and Eleonora Zege for stimulating discussions about MSL theory, technology, and observations. . . from both sides of the clouds. The insightful comments of two anonymous reviewers were greatly appreciated.

References

- American Society for Testing and Materials (2000), *Standard Solar Constant and Air Mass Zero Solar Spectral Irradiance Tables*, Standard E-490-00, West Conshohocken, Pa.
- Barker, H. W. (1996), A parameterization for computing grid-averaged solar fluxes for inhomogeneous marine boundary layer clouds—Part 1, Methodology and homogeneous biases, *J. Atmos. Sci.*, **53**, 2289–2303.
- Barker, H. W., and A. B. Davis (2005), Approximation methods in atmospheric 3D radiative transfer, part 2: Unresolved variability and climate applications, in *3D Radiative Transfer in Cloudy Atmospheres*, edited by A. Marshak and A. B. Davis, chap. 6, pp. 343–383, Springer, Heidelberg, Germany.
- Bissonnette, L., G. Roy, L. Poutier, S. Cober, and G. Isaac (2002), Multiple-scattering lidar retrieval method: Tests on Monte Carlo simulations and comparisons with in situ measurements, *Appl. Opt.*, **41**, 6307–6324.
- Bohren, C. F., J. R. Linsken, and M. E. Churma (1995), At what optical thickness does a cloud completely obscure the Sun?, *J. Atmos. Sci.*, **52**, 1257–1259.
- Cahalan, R. F., M. J. McGill, J. Kolasinski, T. Várnai, and K. Yetzer (2005), THOR, cloud Thickness from Offbeam lidar Returns, *J. Atmos. Oceanic Technol.*, **22**, 605–627.
- Cairns, B., A. W. Lacis, and B. E. Carlson (2000), Absorption within inhomogeneous clouds and its parameterization in general circulation models, *J. Atmos. Sci.*, **57**, 700–714.
- Case, K. M., and P. F. Zweifel (1967), *Linear Transport Theory*, Addison-Wesley, Reading, Mass.
- Chiu, J. C., A. Marshak, W. J. Wiscombe, S. C. Valencia, and E. J. Welton (2007), Cloud optical depth retrievals from solar background signals of micropulse lidars, *IEEE Geosci. Remote Sens. Lett.*, **4**, 456–460.
- Crisp, D., et al. (2004), The Orbiting Carbon Observatory (OCO) mission, *Adv. Space Res.*, **34**, 700–709.
- Davis, A. B., and A. Marshak (2002), Space-time characteristics of light transmitted through dense clouds: A Green's function analysis, *J. Atmos. Sci.*, **59**, 2713–2727.
- Davis, A. B., and A. Marshak (2004), Photon propagation in heterogeneous optical media with spatial correlations: Enhanced mean-free-paths and wider-than-exponential free-path distributions, *J. Quant. Spectrosc. Radiat. Transfer*, **84**, 3–34.
- Davis, A., A. Marshak, R. F. Cahalan, and W. J. Wiscombe (1997), The Landsat scale break in stratocumulus as a three-dimensional radiative transfer effect: Implications for cloud remote sensing, *J. Atmos. Sci.*, **54**, 241–260.
- Davis, A. B., R. F. Cahalan, J. D. Spinhirne, M. J. McGill, and S. P. Love (1999), Off-beam lidar: An emerging technique in cloud remote sensing based on radiative Green-function theory in the diffusion domain, *Phys. Chem. Earth B*, **24**, 177–185. (Erratum, *Phys. Chem. Earth B*, **24**, 757–765, 1999.)
- Davison, B. (1958), *Neutron Transport Theory*, Oxford Univ. Press, London, U. K.
- Deirmendjian, D. (1969), *Electromagnetic Scattering on Spherical Polydispersions*, Elsevier, New York.
- Eriksson, K., D. Estep, P. Hansbo, and C. Johnson (1996), *Computational Differential Equations*, Cambridge Univ. Press, New York.
- Evans, K. F., R. P. Lawson, P. Zmarzly, and D. O'Connor (2003), In situ cloud sensing with multiple scattering cloud lidar: Simulations and demonstration, *J. Atmos. Oceanic Technol.*, **20**, 1505–1522.
- Evans, K. F., D. O'Connor, P. Zmarzly, and R. P. Lawson (2006), In situ cloud sensing with multiple scattering lidar: Design and validation of an airborne sensor, *J. Atmos. Oceanic Technol.*, **23**, 1068–1081.
- Flesia, C., and P. Schwendimann (Eds.) (1995), Special section on Multiple Scattering in Lidar Experiments (MUSCLE), *Appl. Phys. B*, **60**, 315–362.
- Gerber, H., Y. Takano, T. J. Garrett, and P. V. Hobbs (2000), Nephelometer measurements of the asymmetry parameter, volume extinction coefficient, and backscatter ratio in arctic clouds, *J. Atmos. Sci.*, **57**, 3021–3034.
- Ghan, S. J., and S. E. Schwartz (2007), Aerosol properties and processes: A path from field and laboratory measurements to global climate models, *Bull. Am. Meteorol. Soc.*, **88**, 1059–1083.
- Heney, L. C., and J. L. Greenstein (1941), Diffuse radiation in the galaxy, *Astrophys. J.*, **93**, 70–83.
- Hogan, R. J. (2008), Fast lidar and radar multiple-scattering models part 1: Small-angle scattering using the photon variance-covariance method, *J. Atmos. Sci.*, doi:10.1175/2008JAS2642.1, in press.
- Hogan, R. J., and A. Battaglia (2008), Fast lidar and radar multiple-scattering models part 2: Wide-angle scattering using the time-dependent two-stream approximation, *J. Atmos. Sci.*, doi:10.1175/2008JAS2643.1, in press.
- Joseph, J. H., W. J. Wiscombe, and J. A. Weinman (1976), The delta-Eddington approximation for radiative flux transfer, *J. Atmos. Sci.*, **33**, 2452–2459.
- Love, S. P., A. B. Davis, C. Ho, and C. A. Rohde (2001a), Remote sensing of cloud thickness and liquid water content with Wide-Angle Imaging Lidar, *Atmos. Res.*, **59–60**, 295–312.
- Love, S. P., A. B. Davis, C. A. Rohde, and C. Ho (2001b), Wide-Angle Imaging Lidar (WAIL): A ground-based instrument for monitoring the thickness and density of optically thick clouds, *Proc. SPIE Int. Soc. Opt. Eng.*, **4377**, 206–217.
- Marshak, A., A. Davis, W. J. Wiscombe, and R. F. Cahalan (1995), Radiative smoothing in fractal clouds, *J. Geophys. Res.*, **100**, 26,247–26,261.
- Meador, W. E., and W. R. Weaver (1980), Two-stream approximations to radiative transfer in planetary atmospheres: A unified description of existing methods and a new improvement, *J. Atmos. Sci.*, **37**, 630–643.
- Miller, S. D., and G. L. Stephens (1999), Multiple scattering effects in the lidar pulse stretching problem, *J. Geophys. Res.*, **104**, 22,205–22,219.
- Min, Q.-L., and L. C. Harrison (1999), Joint statistics of photon pathlength and cloud optical depth, *Geophys. Res. Lett.*, **26**, 1425–1428.
- Pawlowski, H., et al. (2000), Microphysical and radiative properties of stratocumulus clouds: The EUCREX mission 206 case study, *Atmos. Res.*, **55**, 85–102.

- Pfeilsticker, K., F. Erle, O. Funk, H. Veitel, and U. Platt (1998), First geometrical pathlength distribution measurements of skylight using the oxygen A-band absorption technique: 1. Measurement technique, atmospheric observations, and model calculations, *J. Geophys. Res.*, *103*, 11,483–11,504.
- Platt, C. M. R., W. H. Hunt, D. M. Winker, and M. A. Vaughan (1998), Measurement of cloud solar reflected radiance and extinction from space lidar, *Proc. SPIE Int. Soc. Opt. Eng.*, *3504*, 542–545.
- Polonsky, I. N., and A. B. Davis (2004), Lateral photon transport in dense scattering and weakly absorbing media of finite thickness: Asymptotic analysis of the space-time Green function, *J. Opt. Soc. Am. A*, *21*, 1018–1025.
- Polonsky, I. N., S. P. Love, and A. B. Davis (2005), Wide-Angle Imaging Lidar deployment at the ARM Southern Great Plains site: Intercomparison of cloud property retrievals, *J. Atmos. Oceanic Technol.*, *22*, 628–648.
- Schuster, A. (1905), Radiation through a foggy atmosphere, *Astrophys. J.*, *21*, 1–22.
- Solomon, S., D. Qin, and M. Manning (Eds.) (2007), *Climate Change 2007: The Physical Science Basis*, Intergovt. Panel on Clim. Change, Geneva, Switzerland.
- Spinhirne, J. D. (1993), Micropulse lidar, *IEEE Trans. Geosc. Remote Sens.*, *31*, 48–55.
- Stephens, G. L. (1994), *Remote Sensing of the Lower Atmosphere: An Introduction*, Oxford Univ. Press, New York.
- Winker, D. M., R. H. Couch, and M. P. McCormick (1996), An overview of LITE: NASA's Lidar In-space Technology Experiment, *Proc. IEEE*, *84*, 164–180.
- Yang, Y., et al. (2008), Retrievals of thick cloud optical depth from the Geoscience Laser Altimeter System (GLAS) by calibration of solar background signal, *J. Atmos. Sci.*, doi:10.1175/2008JAS27441, in press.

A. B. Davis, Space and Remote Sensing Group (ISR-2), Los Alamos National Laboratory, Mail Stop B-244, Los Alamos, NM 87545, USA. (adavis@lanl.gov)